Electrochemistry Communications 123 (2021) 106927

Contents lists available at ScienceDirect

Electrochemistry Communications

journal homepage: www.elsevier.com/locate/elecom

Full Communication

Monitoring amyloid-β 42 conformational change using a spray-printed graphene electrode

Bing Li [a,b,*], Guohui Zhang [c], Islam Bogachan Tahirbegi [a,b], Michael J. Morten [a,d], Haijie Tan [e]

[a] Department of Brain Sciences, Imperial College London, W12 0NN, UK
[b] UK Dementia Research Institute Care Research & Technology Centre, Imperial College London and University of Surrey, W12 0NN, UK
[c] Department of Chemistry, Imperial College London, W12 0BZ, UK
[d] UK Dementia Research Institute at Imperial College London, W12 0NN, UK
[e] Hamlyn Centre, Department of Computing, Imperial College London, SW7 2AZ, UK

ARTICLE INFO

Keywords:
Reduced graphene oxide
Spray-printing
Electrochemical sensor
Neurodegenerative disease
Protein aggregation

ABSTRACT

Up to now, the reproducibility and stability of graphene-based electrochemical sensors have represented an obstacle to the development of practical biosensing techniques. In this paper we report a cost-effective and highly reproducible graphene-based electrochemical sensing platform to monitor the kinetic conformational change of amyloidogenic proteins. The sensor surface is spray-printed with a graphene oxide layer and then electrochemically reduced to achieve excellent sensitivity to the redox current. The reproducibility of these sensors in terms of redox peak position, intensity and electroactive area has been proved to be high. These sensors are used to monitor the conformational changes of amyloid-β 42 via the change in the oxidation current of tyrosine, which is caused by different electrochemical accessibility during the aggregation process. The aggregation process detected at these graphene electrochemical sensors shows a good correlation with the fluorescence assay. The proposed platform provides a complementary technique to aid understanding of the detailed process of amyloidogenic protein aggregation and the mechanism of neurodegenerative diseases as well as helping to promote the development of disease-prevention strategies.

1. Introduction

Aggregation of amyloidogenic proteins, which is induced by an imbalance in the production and clearance of β-sheet polypeptide structures, is a pathological process implicated in neurodegenerative disease. However, from monomeric peptide to mature fibrils, it remains unclear how many intermediates are produced, and which specific form is most toxic to neural cells [1]. Therefore, an understanding of the detailed aggregation process of these proteins is clinically important for the development of disease-modifying and preventive strategies for neurodegenerative disease [2]. Current gold-standard methods for studying protein aggregation include fluorescence microscopy, transmission electron microscopy, atomic force microscopy and size-exclusion chromatography [3–5]. However, these rely on demanding laser or electron beam excitation techniques and a complex signal capture system to monitor the formation of oligomeric peptides at the later stage of aggregation. A complementary label-free, ultrasensitive and rapid technique would be useful for monitoring the onset of misfolding intermediates with low steady concentrations.

Electrochemical sensors can be operated on a simple potentiostat in a real-time and label-free manner without perturbing the protein conformation during the measurements, providing additional advantages over current analytical methods. Exploratory works have been performed using standard glassy carbon and gold electrodes to study the tau/metal ion interaction [6], the binding of monomers to pre-immobilised tau seeds [7] and the kinetic conformational change of Amyloid-β (Aβ) [8]. To provide a more in-depth understanding of the aggregation of amyloidogenic proteins, different nanomaterials have been integrated into the electrochemical sensors to enhance their sensing performance [9–12]. As one of the most promising candidates for developing ultrasensitive electrodes, graphene offers an intrinsically high surface-to-volume ratio, high electrochemical activity and lone-pair π electrons suspended on top of its surface [13,14]. This makes graphene electrodes sensitive to the accumulation of electrons caused by protein adsorption [15] and aggregation [16], and the redox current change caused by the conformational change of electroactive protein molecules on its surface.

* Corresponding author at: Department of Brain Sciences, Imperial College London, W12 0NN, UK.
E-mail address: b.li@imperial.ac.uk (B. Li).

https://doi.org/10.1016/j.elecom.2021.106927
Received 12 December 2020; Received in revised form 28 December 2020; Accepted 9 January 2021
Available online 16 January 2021

However, the reproducibility of the electrochemical performance of graphene-based single-use sensors has not yet been well addressed. Furthermore, the conformational change of the amyloidogenic protein has never been experimentally studied using this electrochemical sensing platform.

In this work, a cost-effective, highly reproducible and ultrasensitive reduced graphene oxide (rGO) electrochemical sensor for the kinetic study of amyloidogenic protein aggregation has been developed using a spray-printing technique. High reproducibility of these sensors in terms of peak position, intensity and electroactive area has been observed in the ferricyanide system. The sensing mechanism is that the electroactive amino acids in a peptide, such as tyrosine (Tyr), tryptophan and cysteine, receive or donate electrons at specific electrical potentials, which define redox peaks in electrochemical measurements. Any conformational changes of peptides are expected to affect the spatial location of these amino acids relative to the electrode surface, which subsequently changes their electrochemical accessibility and results in a change in the redox current. Aβ42 is chosen as a representative amyloidogenic protein – it is a marker for Alzheimer's disease (AD) when produced in excess and aggregated onto neural cells. Also, the Aβ42 monomer possesses only one redox active Tyr residue at position 10 from the N-terminal, offering the simplest correlation between its oxidation currents and conformational change. The electrochemical results are cross-validated using a ProteoStat aggresome detection kit.

2. Results and discussion

2.1. Sensing mechanism

Soluble Aβ42 monomers in the brain and cerebrospinal fluid aggregate to form plaques in the brains of AD patients. The aggregation starts from an unfolded state consisting of an α-helix or random coil structure, then undergoes a multi-step nucleated polymerisation process, which involves the formation of β-sheet structures, soluble oligomeric intermediates of different size and forms, and eventually ends with insoluble fibrils [17], as shown in Fig. 1. Tyr, the only oxidizable residue at around 0.6 V in Aβ42, is wrapped by other amino acids and located in a continuously changing spatial position relative to the electrode surface during the aggregation process. This leads to a change in its electrochemical accessibility, which enables the electrochemical monitoring of Aβ42 aggregation by analysing the corresponding oxidation current intensity at different stages.

2.2. Optimisation of spray-printed rGO electrodes

One of the most critical requirements for the development of electrochemical sensors is to determine the optimal thickness of rGO to provide good electrochemical reversibility and uniformity, which can be evaluated by the ratio of cathodic and anodic peak currents, I_{pc}/I_{pa} [18]. Fig. 2(a) shows the cyclic voltammetric (CV) characteristics of electrodes modified with different volumes of GO solution (0 to 0.6 mL) in 5 mM potassium ferricyanide ($K_3[Fe(CN)_6]$), which is an outer-sphere redox mediator and proceeds via a single electron transfer pathway. The fabrication process is detailed in the Supplementary Information, section 1.2. The reduction peaks decrease from 165 μA to 0.571 μA (a decrease of 99.6%), while the oxidation peaks decrease from 163 μA to 2.09 μA (a decrease of 98.7%), along with a decrease in the electroactive area from 7.11 to 0.02 mm^2, indicating that the working electrode has been covered by an insulating GO layer. However, a GO layer which exceeds the optimal thickness will lead to a degradation in the electrochemical reversibility and film uniformity, which is indicated by increasing peak-to-peak separation as a function of GO volume. To find the optimal thickness, GO volumes are plotted against I_{pc}/I_{pa} in Fig. 2(b), which shows that I_{pc}/I_{pa} starts to decrease when more than 0.2 mL GO is sprayed, when I_{pc}/I_{pa} drops from 1.02 to 0.96. Therefore, 0.2 mL GO is used for the fabrication of homogeneous GO layers on the working electrodes without them losing their uniformity and electrochemical reversibility in the $K_3[Fe(CN)_6]$ system.

High reproducibility of the electrodes is the most important requirement for the development of reliable electrochemical sensors. This ensures that single-use sensors are exposed to the adsorption of Aβ42 from the same baseline and makes the comparison of sensing results from different electrodes meaningful. Fig. 2(c) presents the CV characteristics of 15 individual rGO-modified electrodes fabricated and electrochemically reduced using the same parameters. By controlling the quality of the GO solution, the volume of sprayed GO solution and the number of CV scans, electrodes with high reproducibility can be obtained. Statistically, the standard deviations (STD) of reduction peak potentials, peak currents and peak areas were found to be 20%, 1.82% and 1.3%, respectively, which are within the usual range for differences in commercial electrodes, as shown in Fig. 2(d).

2.3. Characterisation of the rGO electrode surface

The formation of a GO film and its electrochemical reduction are first characterised using Raman spectroscopy. Fig. 3(a) shows a comparison of spectra from a GO-modified electrode before and after the reduction process, with reference to a graphene-nanosheet-modified electrode. Both GO and rGO present increased D bands, the increased intensity ratio of D to G bands (I_D/I_G) and the flattened 2D band indicating that a large number of defective sites have been introduced into the electrode surface [19]. The I_D/I_G ratio is also discriminative for the average

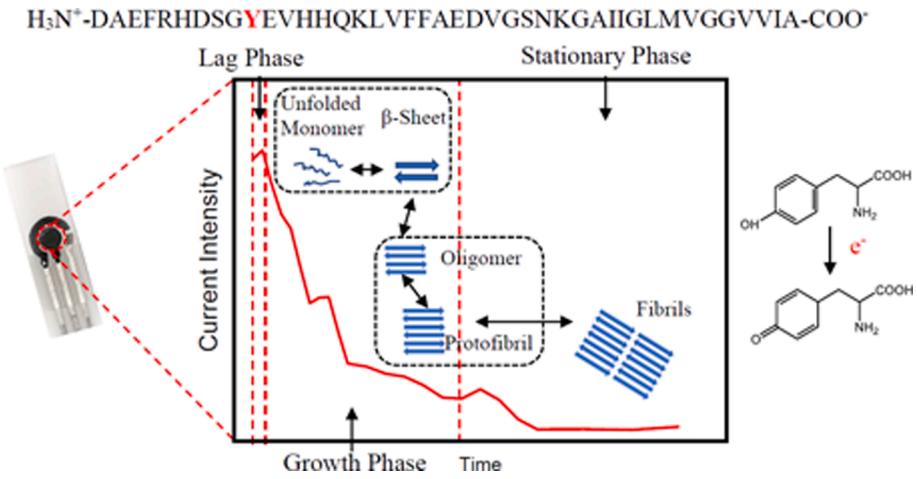

Fig. 1. Mechanism for monitoring Aβ42 conformational change using an electrochemical sensor.

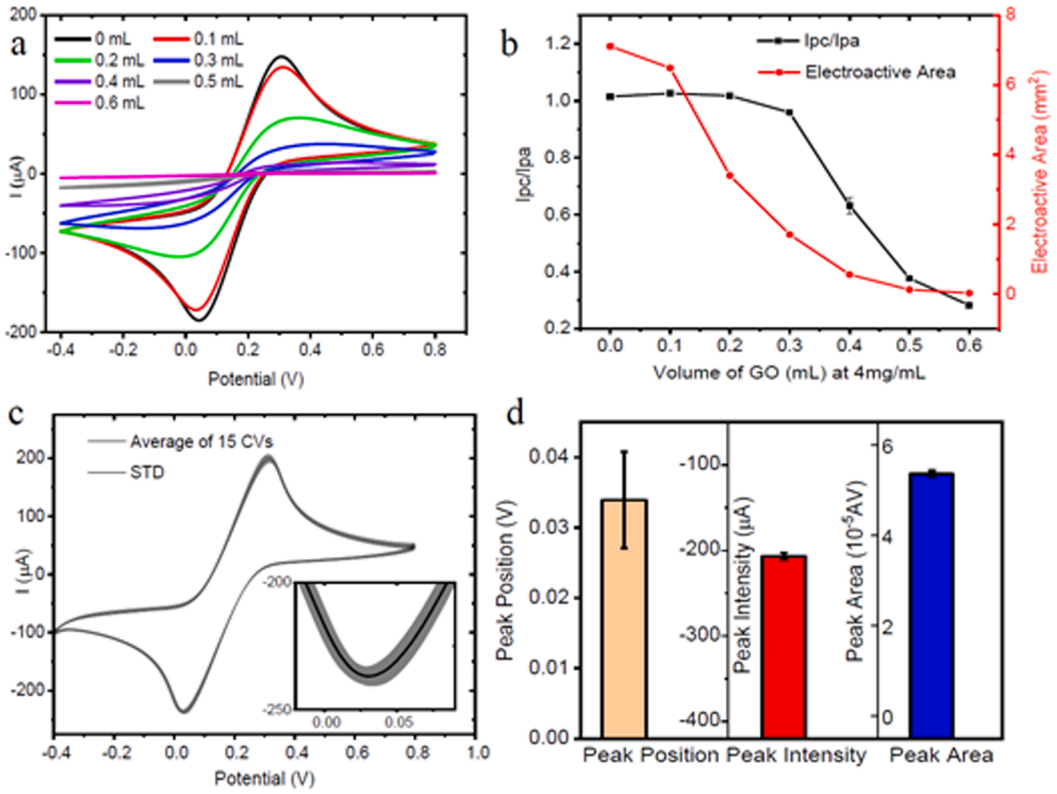

Fig. 2. Optimisation of GO thickness and analysis of electrode reproducibility. (a) CVs of electrodes modified with different volumes of GO ranging from 0 to 0.6 mL, recorded in 5 mM $K_3[Fe(CN)_6]$ at a scan rate of 100 mV s^{-1}. (b) Analysis of the I_{pc}/I_{pa} ratio and electroactive area versus the sprayed GO volume. (c) CVs from 15 individual rGO-modified devices with a scan rate of 100 mV s^{-1} (inset: expansion of the reduction peak region). (d) Standard deviations for redox peak potentials, peak currents and integral peak areas.

distance (L_D) between defective sites [20]. This ratio increases with an increase in L_D from 0 to 3 nm, peaks at 3–4 nm, and then decreases with a further increase in L_D. As the L_D for GO is around 1 nm and chemical moieties have been partially removed during the reduction process, the L_D has consequently increased, leading to an increase in I_D/I_G from 0.92 to 1.29. No pinholes (areas not covered by graphene) can be observed from the 2D and 3D G band intensity maps (Fig. 3(b) and (c)) and the intensities show a narrow distribution in the statistical histogram, indicating a uniform rGO layer.

Fig. 3(d) and (e) show the scanning electron microscopy (SEM) images of a GO-modified electrode before and after the reduction process. Due to the significantly increased electrical conductivity of rGO, the contrast in Fig. 3(e) is sharper when both images are taken at the same beam power. In addition, both SEM images confirm that the surface coverage is nearly 100%, which is in consistent with the Raman analysis. The surface shows a uniform morphology at the electrode scale (as shown in Fig. S3). The removal of oxygen-containing moieties is semi-quantitatively determined by X-ray photoelectron spectroscopy (XPS), as shown in Fig. 3(f). Wide-range spectra from GO and rGO both contain carbon peaks at 285 eV and oxygen peaks at 532 eV. However, from the corresponding sensitivities, it can be deduced that the atomic ratio of oxygen decreases from 25.05% to 10.05% after the electrochemical reduction. This is close to the 6.56% measured with a pristine graphene electrode as shown in Fig. S2. The corresponding high-resolution C1s spectra are presented in the insets to Fig. 3(f). The C1s spectrum from GO includes three major peaks at 284.45 eV, 286.58 eV and 288.38 eV, corresponding to the C–C bonds in the graphene lattice (62.96%), the C-O bond in alkoxy and epoxy groups (32.83%) and the C=O bond in carboxyl groups (4.21%), respectively [21]. By comparison, all the peaks corresponding to oxygen-containing moieties have decreased in the C1s spectrum obtained from rGO, especially the peak at 286.58 eV (to 3.52%), showing the removal of a significant amount of alkoxy and epoxy groups.

2.4. Electrochemical performance of spray-printed rGO electrode

Fig. 4(a) shows a comparison of the CVs obtained in the $K_3[Fe(CN)_6]$ system from three electrodes modified with carbon, GO and rGO. The CV from the carbon electrode shows an I_{pc} of −170 μA, which decreases to −25.2 μA after the deposition of GO and later increases to −233 μA upon the reduction of GO. The increased peak currents indicate the enhanced electroactivity of the rGO layer as the working electrode. Using the Randles-Sevcik equation, it can be calculated that this represents an increased electroactive area of 2.7 mm^2 within the confined electrode pattern. Meanwhile, the potential separation between the reduction and oxidation peaks decreases from 0.25 V (carbon) to 0.22 V (rGO), representing faster electron transfer kinetics at the electrode surface. This is because the electron transport takes place via both graphene planes [22] and the defective sites within the rGO layer [13], which are inherited from the GO layer on the removal of the insulating oxygen-containing moieties. The introduction of these additional electroactive sites leads to a larger electroactive area for donating or receiving electrons during the ferricyanide redox processes, which in turn results in enhanced currents.

Fig. 4(b) shows CVs recorded at different scan rates (from 10 to 200 mV/s) on a rGO-modified electrode. All CVs show highly symmetric redox currents, but the separation between redox peaks increases with the increase in the scan rate, indicating a quasi-reversible electrochemical process. The intensities of the redox peaks have a linear relationship with the corresponding square root of the scan rate, as shown in Fig. 4(c), demonstrating a diffusion-controlled electrochemical reaction without $K_3[Fe(CN)_6]$ adsorption on the electrode, which is important for

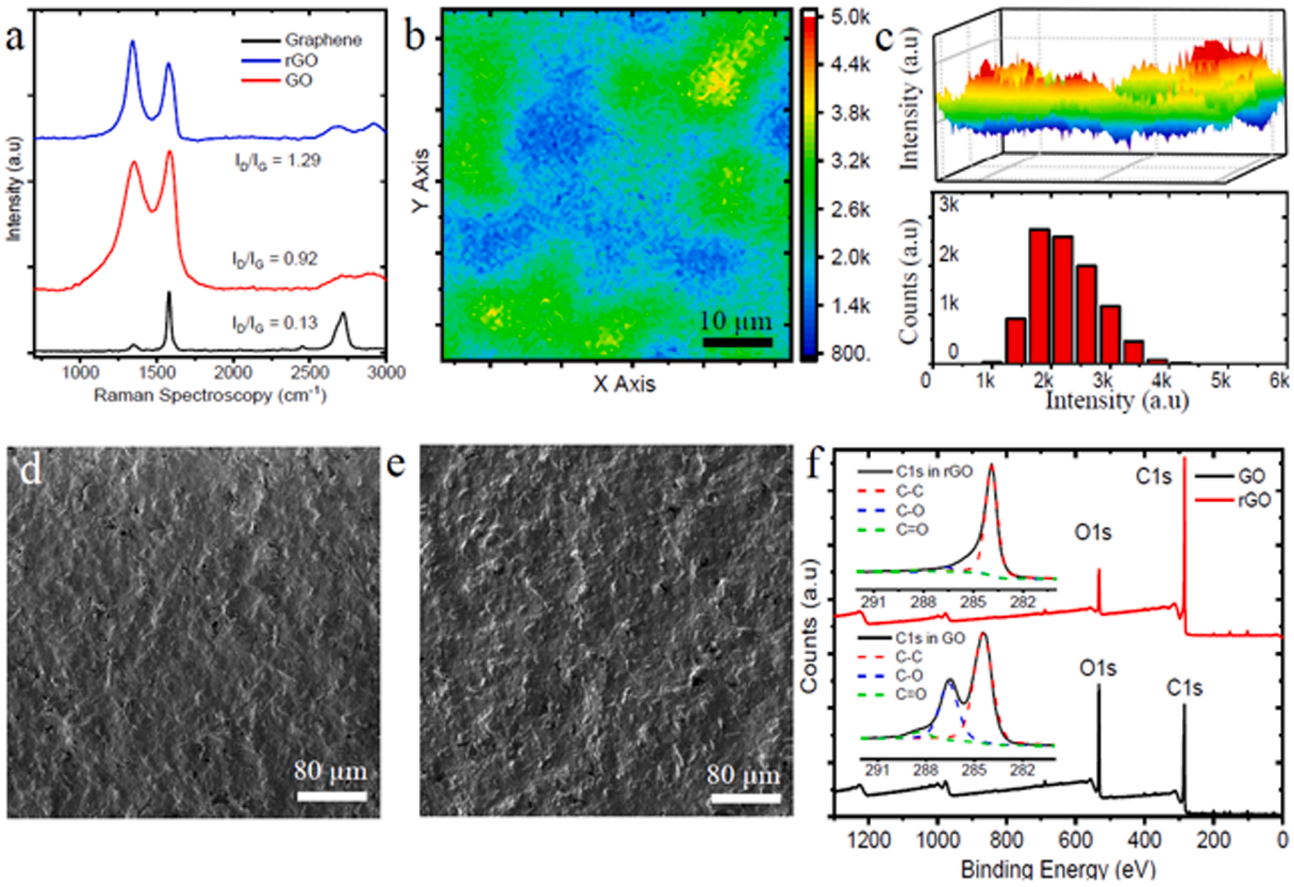

Fig. 3. Characterisation of GO- and rGO-modified electrodes. (a) Raman spectra from electrodes modified with graphene nanosheets, GO and rGO. (b) 2D G-band Raman mapping across 50 × 50 μm on the rGO electrode. (c) 3D G-band mapping and statistical histogram of intensity distribution, indicating the rGO coverage is 100% and the film is homogeneous. (d-e) SEM images of a GO-modified electrode before and after the electrochemical reduction process, showing the uniform electrode surface morphology. (f) XPS analysis of GO and rGO electrodes. Inset: high-resolution spectra of the C1s region and corresponding peak fittings.

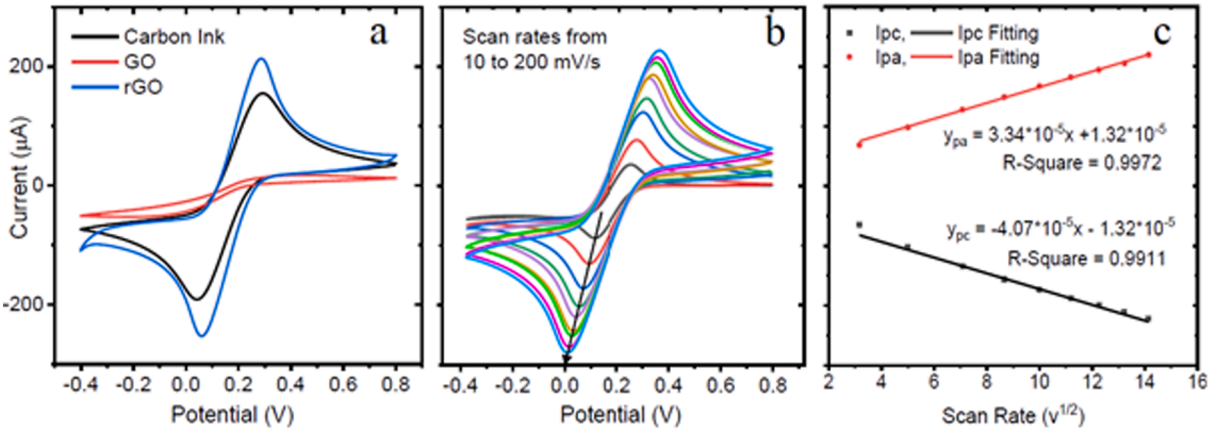

Fig. 4. Electrochemical performance of rGO-modified electrodes in 5 mM $K_3[Fe(CN)_6]$. (a) CVs of electrodes modified with carbon ink, GO and rGO with a scan rate of 100 mV/s. (b) CVs of a rGO-modified electrode recorded at different scan rates (10, 25, 50, 75, 100, 125, 150, 175 and 200 mV/s). The scan rate increases in the direction of the arrow. (c) Cathodic and anodic currents vs the square root of the corresponding scan rate.

the development of electrochemical biosensors.

2.5. Monitoring of Aβ42 aggregation using electrochemical sensors

CV and differential pulse voltammetry (DPV) have been used to study the electrochemical oxidation of Tyr on rGO-modified electrodes. Fig. 5(a) shows enlarged details of CV scans from a bare rGO electrode and a rGO electrode modified with 50 μM Aβ42 in phosphate-buffered saline (PBS) solution. Compared with the CV from the rGO electrode, the CV from Aβ42-modified rGO electrode has a Tyr oxidation peak at 0.583 V, which is close to the free Tyr oxidation peak at 0.62 V in Fig. S4, but less positive than the oxidation potential reported in the literature [23,24]. The mechanism of Tyr oxidation depends on the electrode materials, solution pH and composition. For scans performed under

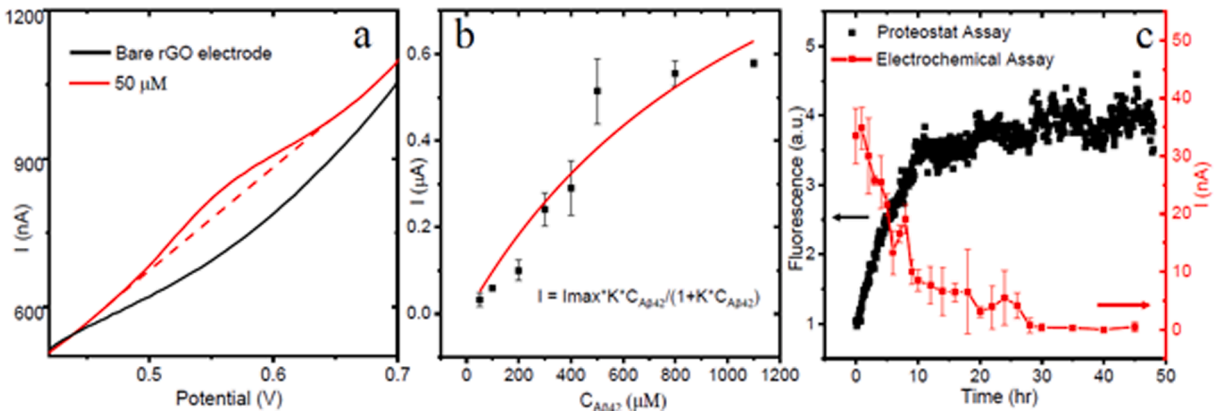

Fig. 5. Electrochemical monitoring of Aβ42 oxidation and aggregation. (a) Enlarged detail of CVs from a 50 μM Aβ42-modified rGO electrode and a bare rGO electrode in PBS. (b) Dependence of the oxidation peak current on the concentration of Aβ42 monomer on the electrode surface, fitted using the Langmuir isotherm (red solid line). (c) Correlation between the electrochemical oxidation current (right *y* axis) and the fluorescence signal (left *y* axis) at different stages of aggregation. (For interpretation of the references to colour in this figure legend, the reader is referred to the web version of this article.)

moderate oxidation conditions in a neutral PBS buffer, Tyr molecules are oxidised via a one-electron process, as shown in Fig. 1, providing a very simple model for correlation of oxidation peak currents with conformational changes. Fig. 5(b) shows the electrochemical oxidation currents obtained with different concentrations of Aβ42 adsorbed on the rGO-modified electrodes. Each concentration of Aβ42 is measured using a freshly prepared rGO electrode to ensure the baselines are constant. The oxidation peak current increases with the increase in Aβ42 concentration and starts to saturate after 400 μM. A concentration of 50 μM has been found to be optimal to ensure that more physically adsorbed Aβ42 monomers stay on the surface of electrode and contribute to the electrochemical oxidation current, while the oxidation peak is identifiable in CV scans. By fitting Fig. 5(b) using the Langmuir isotherm $I = I_{Max} \times K \times C_{A\beta}/(1 + K \times C_{A\beta})$ [25], the values of I_{Max} and the equilibrium constant K have been found to be 1.37 μA and 7.74×10^{-4}, respectively, which indicates a weak binding between the Aβ42 monomer and the rGO electrode. The surface amount of Aβ42 at the chosen concentration (50 μM) at rGO-modified electrodes ($d = 4$ mm) has been calculated to be 6.83 pmol using $\Gamma = Q/nFA$ [26], where Q is the total charge, n is the number of electrons, F is the Faraday constant and A is the surface area of the working electrode. Meanwhile, the saturated density of Aβ42 has been calculated to be 120 pmol, indicating a loosely packed Aβ42 monomer layer when 50 μM is used.

Conformational changes of Aβ42 during fibrillation have been characterised using both electrochemical sensors and a fluorescence assay, as shown in Fig. 5(c). For the electrochemical study, Aβ42 aggregation is monitored at a concentration of 50 μM. This ensures the peptide adsorption is unsaturated and all peptides present same initial spatial position to the rGO surface. With an increase in aggregation time, the Tyr oxidation current gradually decreases, reaches its minimum value and becomes less identifiable after 30 hrs, due to the decreased number of Tyr that can contribute to the electrochemical oxidation. The two major fluctuations after 8 and 24 hrs may be attributed to the formation of transitional oligomer and protofibril, which leads to an increase in the electrochemical accessibility of Tyr for short periods. To validate the electrochemical characterisation, a ProteoStat fluorescence assay (as detailed in the Supplementary Information, section 1.4), a gold-standard analytical method for studying protein aggregation, is performed with the same concentration of Aβ42 and the fluorescence signals are plotted over the same time scale in Fig. 5(c). At the beginning ($t = 0$), where the electrochemical current from Aβ42 monomer oxidation has its maximum value, the fluorescence assay shows minimum background fluorescence, since no β-sheet structure has formed at this stage. With the alignment of monomers into β-sheet structures over time, the fluorescence intensity increases linearly with amyloid fibril mass in the first 10 hrs, reaching a plateau after 30 hrs, which correlates well with the electrochemical analysis. Since the ProteoStat assay detects the formation of β-sheet intermediates, the fluorescence signals are inversely in proportional to Tyr oxidation current throughout the aggregation process. The lag phase of the fluorescence assay in this work is very short compared to other published results. This is mainly attributed to the higher monomer concentration of Aβ42 and the pre-treatment with 1,1,1,3,3,3-hexafluoro-2-propanol (see Supplementary Information), both of which could cause faster aggregation and β-sheet formation [27–29].

3. Conclusion

This work reports a spray-printing technique for the development of rGO-based electrodes, which offers high reproducibility in the reduction peak potentials, peak currents and peak areas with STDs of 20%, 1.82% and 1.3%, respectively, in the $K_3[Fe(CN)_6]$ system. The uniform surface morphology is shown by SEM and Raman spectroscopy, while the increased electrochemical activity and the diffusion-controlled behaviour are demonstrated in electrochemical analysis, making the electrodes good electrochemical sensors. The sensors are used to monitor the kinetic Aβ42 aggregation process via the consecutive changing oxidation current of Tyr in Aβ42, which correlates well with the fluorescence assay throughout all of the aggregation phases. This shows the potential of highly reproducible rGO electrodes in studying the aggregation process of amyloidogenic proteins, and may promote the study of unstable transition phases of oligomers as a complementary technique to state-of-the-art laser-based assays.

CRediT authorship contribution statement

Bing Li: Conceptualization, Methodology, Investigation, Formal analysis, Data curation, Writing - original draft, Writing - review & editing, Validation, Supervision, Project administration, Funding acquisition. **Guohui Zhang:** Formal analysis, Methodology, Writing - original draft, Writing - review & editing. **Islam Bogachan Tahirbegi:** Methodology, Investigation, Data curation, Writing - original draft, Writing - review & editing. **Michael J. Morten:** Methodology, Investigation, Data curation, Writing - original draft, Writing - review & editing. **Haijie Tan:** Investigation, Writing - review & editing.

Declaration of Competing Interest

The authors declare that they have no known competing financial interests or personal relationships that could have appeared to influence

the work reported in this paper.

Acknowledgement

This work is supported by the Edmond J. Safra Foundation (Edmond and Lily Safra Research Fellow to Bing Li) and the UK Dementia Research Institute (funded by UK Medical Research Council, Alzheimer's Society and Alzheimer's Research UK). We thank Dr Kerherve (APSL) at Imperial College London for the XPS support.

Appendix A. Supplementary data

Supplementary data to this article can be found online at https://doi.org/10.1016/j.elecom.2021.106927.

References

[1] I. Benilova, E. Karran, B. De Strooper, Nat. Neurosci. 15 (2012) 349–357.
[2] J. Vaquer-Alicea, M.I. Diamond, Annu. Rev. Biochem. 88 (2019) 785–810.
[3] T.C.T. Michaels, A. Šarić, S. Curk, K. Bernfur, P. Arosio, G. Meisl, A.J. Dear, S.I. A. Cohen, C.M. Dobson, M. Vendruscolo, S. Linse, T.P.J. Knowles, Nat. Chem. 12 (2020) 445–451.
[4] S.L. Shammas, G.A. Garcia, S. Kumar, M. Kjaergaard, M.H. Horrocks, N. Shivji, E. Mandelkow, T.P.J. Knowles, E. Mandelkow, D. Klenerman, Nat. Commun. 6 (2015) 7025.
[5] F. Kundel, S. De, P. Flagmeier, M.H. Horrocks, M. Kjaergaard, S.L. Shammas, S. E. Jackson, C.M. Dobson, D. Klenerman, ACS Chem. Biol. 13 (2018) 636–646.
[6] S. Martic, M.K. Rains, H.-B. Kraatz, Anal. Biochem. 442 (2013) 130–137.
[7] J.O. Esteves-Villanueva, H. Trzeciakiewicz, S. Martic, Analyst 139 (2014) 2823–2831.
[8] M.D. Vestergaard, K. Kerman, M. Saito, N. Nagatani, Y. Takamura, E. Tamiya, J. Am. Chem. Soc. 127 (2005) 11892–11893.
[9] N. Xia, X. Wang, B. Zhou, Y. Wu, W. Mao, L. Liu, ACS Appl. Mater. Interfaces 8 (2016) 19303–19311.
[10] V.W.-S. Hung, H. Masoom, K. Kerman, J. Electroanal. Chem. 681 (2012) 89–95.
[11] M. Masařík, A. Stobiecka, R. Kizek, F. Jelen, Z. Pechan, W. Hoyer, T.M. Jovin, V. Subramaniam, E. Paleček, Electroanalysis 16 (2004) 1172–1181.
[12] E. de la Fuente, C. Adura, M.J. Kogan, S. Bollo, Electroanalysis 24 (2012) 938–944.
[13] B. Li, G. Pan, N.D. Avent, R.B. Lowry, T.E. Madgett, P.L. Waines, Biosens. Bioelectron. 72 (2015) 313–319.
[14] B. Li, G. Pan, N.D. Avent, K. Islam, S. Awan, P. Davey, J. Nanosci. Nanotechnol. 16 (2016) 12805–12810.
[15] S. Taniselass, M.K.M. Arshad, S.C.B. Gopinath, Biosens. Bioelectron. 130 (2019) 276–292.
[16] A. Vasilescu, S. Boulahneche, F. Chekin, S. Gáspár, M.S. Medjram, A.A. Diagne, S. K. Singh, S. Kurungot, R. Boukherroub, S. Szunerits, Electrochim. Acta 254 (2017) 375–383.
[17] A. Jan, D.M. Hartley, H.A. Lashuel, Nat. Protoc. 5 (2010) 1186–1209.
[18] M.M.S. Silva, A.C.M.S. Dias, B.V.M. Silva, S.L.R. Gomes-Filho, L.T. Kubota, M.O. F. Goulart, R.F. Dutra, J. Chem. Technol. Biotechnol. 90 (2015) 194–200.
[19] H.J. Kim, S.-M. Lee, Y.-S. Oh, Y.-H. Yang, Y.S. Lim, D.H. Yoon, C. Lee, J.-Y. Kim, R. S. Ruoff, Sci. Rep. 4 (2014) 5176.
[20] S. Eigler, C. Dotzer, A. Hirsch, Carbon 50 (2012) 3666–3673.
[21] R. Al-Gaashani, A. Najjar, Y. Zakaria, S. Mansour, M. Atieh, Ceram. Int. 45 (2019) 14439–14448.
[22] G. Zhang, P.M. Kirkman, A.N. Patel, A.S. Cuharuc, K. McKelvey, P.R. Unwin, J. Am. Chem. Soc. 136 (2014) 11444–11451.
[23] A. Loksztejn, W. Dzwolak, P. Krysiński, Bioelectrochemistry 72 (2008) 34–40.
[24] G.-P. Jin, X.-Q. Lin, Electrochem. Commun. 6 (2004) 454–460.
[25] P. Lopes, H. Dyrnesli, N. Lorenzen, D. Otzen, E.E. Ferapontova, Analyst 139 (2014) 749–756.
[26] B. Li, M. Famili, E. Pensa, I. Grace, N.J. Long, C. Lambert, T. Albrecht, L.F. Cohen, Nanoscale 10 (2018) 19791–19798.
[27] M. Verma, A. Vats, V. Taneja, Ann. Indian Acad. Neurol. 18 (2015) 138.
[28] Y. Liu, T. Wang, A.N. Calabrese, J.A. Carver, S.F. Cummins, J.H. Bowie, Peptides 73 (2015) 1–6.
[29] T.M. Ryan, J. Caine, H.D. Mertens, N. Kirby, J. Nigro, K. Breheney, L. J. Waddington, V.A. Streltsov, C. Curtain, C.L. Masters, B.R. Roberts, PeerJ. 1 (2013), e73.